SANDIA REPORT

SAND2023-02636
Printed April 2023

Sandia National Laboratories

Predictive Capability Maturity Model Demonstration for Cylindrical Cavity Coupling Using Gemma in the Next Generation Workflow

Prepared by
Sandia National Laboratories
Albuquerque, New Mexico 87185
Livermore, California 94550

Issued by Sandia National Laboratories, operated for the United States Department of Energy by National Technology & Engineering Solutions of Sandia, LLC.

Available to DOE and DOE contractors from

U.S. Department of Energy
Office of Scientific and Technical Information
P.O. Box 62
Oak Ridge, TN 37831

Telephone: (865) 576-8401
Facsimile: (865) 576-5728
E-Mail: reports@osti.gov
Online ordering: http://www.osti.gov/scitech

Available to the public from

U.S. Department of Commerce
National Technical Information Service
5301 Shawnee Road
Alexandria, VA 22312

Telephone: (800) 553-6847
Facsimile: (703) 605-6900
E-Mail: orders@ntis.gov
Online order: https://classic.ntis.gov/help/order-methods

ABSTRACT

The predictive capability maturity model (PCMM) uses the expert elicitation process to generate credibility evidence for a particular analysis. To ensure Gemma has the capability to efficiently produce this credibility evidence, next generation workflows (NGW) are created for the solution verification, calibration/validation, and input uncertainty quantification portions of the PCMM assessment. These workflows are then used on the Higgins cylinder problem, which is representative of applications involving external-to-internal electromagnetic field coupling through a slot. The uncertainties calculated using these workflows are then used to calculate the validation comparison error and the validation uncertainty for the model following the American Society of Mechanical Engineers (ASME) verification and validation (V&V) 20 standard. These workflows will enable analysts to iterate each element of PCMM more efficiently than if completed without using a NGW workflow. An example of this iterative process is shown in Section 7.2.

ACKNOWLEDGMENT

The authors would like to thank George Orient for helping with the creation of the NGW files. Additionally, we would like to thank Maher Salloum for generating a portion of the mesh convergence data in Section 7.

CONTENTS

LIST OF FIGURES

LIST OF TABLES

NOMENCLATURE

ASME American Society of Mechanical Engineers

CEE Common Engineering Environment

CFIE Combined Field Integral Equation

EFIE Electric Field Integral Equation

EM Electromagnetic

HPC High-Performance Computing

MFIE Magnetic Field Integral Equation

NGW Next-Generation Workflow

PCMM Predictive Capability Maturity Model

PIRT Phenomenon Identification and Ranking Table

QoI Quantity of Interest

SME Subject Matter Expert

V&V Verification and Validation

VVUQ Verification, Validation, and Uncertainty Quantification

1. INTRODUCTION TO PCMM

Gemma is a computational electromagnetics code developed by Sandia National Laboratories for the analysis of electromagnetic (EM) coupling and scattering in nuclear deterrence applications. To ensure the proper modeling of such high-consequence systems, credibility of the modeling approach must be rigorously assessed. One way of assessing model credibility is to apply the predictive capability maturity model (PCMM).

A PCMM is constructed based on input from subject matter experts assessing the model itself as well as available verification, validation, and uncertainty quantification (VVUQ) for the model [19]. More specifically, a PCMM examines credibility evidence for a numerical model using six separate elements: code verification, representation and geometric fidelity, physics and material model fidelity, solution verification, validation, and uncertainty quantification (UQ). This report demonstrates the use of the Next-Generation Workflow (NGW) tool to assess three of the more quantitative PCMM elements for a problem similar to those for which Gemma will be used in a production environment. These workflows provide a straightforward way for analysts to set up Gemma simulations and post-process results for accurate VVUQ assessments. The resulting uncertainty metrics can then be combined using the American Society of Mechanical Engineers (ASME) verification and validation (V&V) 20 methodology [2].

Further detail on ASME V&V 20 is given in Section 1.1. The problem used to demonstrate the VVUQ workflows is described in Section 2. The workflows themselves are illustrated in Section 3. Sections 4–9 discuss the assessment of the PCMM elements for the problem of interest and include results generated by the workflows for solution verification (Section 7), validation (Section 8), and uncertainty quantification (Section 9).

1.1. ASME V&V 20 Standard Methodology

The ASME V&V 20 standard is a methodology to assess accuracy of a computational simulation. While the standard focuses on the application of computational fluid dynamics and computational heat transfer, the methodology is applicable to all physics disciplines. The standard quantifies the validation comparison error and bounds it with a validation uncertainty. The validation comparison error E is defined as

$$E = S - D = (T + \delta_S) - (T + \delta_D) = \delta_S - \delta_D, \tag{1.1}$$

where S is the simulation result, D is the experimental data, T is some unknown truth value, δ_S is $S - T$, and δ_D is $D - T$. The simulation error δ_S is made up of the following contributions,

$$\delta_S = \delta_{\text{model}} + \delta_{\text{num}} + \delta_{\text{input}} \tag{1.2}$$

where δ_{model} is the modeling error, δ_{num} is the error from numerical sources, and δ_{input} is the error from incorrect input. Rearranging (1.1) and (1.2) allows the modeling error to be expressed as

$$\delta_{\text{model}} = E - \left(\delta_{\text{num}} + \delta_{\text{input}} - \delta_{\text{D}}\right). \tag{1.3}$$

Unfortunately, these errors cannot be measured. Instead, the errors can be bounded by uncertainties computed in the PCMM. Additionally, the ASME V&V 20 standard indicates that the modeling error is bounded by the validation uncertainty u_{val} which is a combination of numerical uncertainty u_{num} input uncertainty, u_{input}, and experimental uncertainty u_{exp} as

$$u_{\text{val}} = \sqrt{\underbrace{u_{\text{num}}^2}_{\substack{\text{Solution}\\ \text{Verification}}} + \underbrace{u_{\text{input}}^2}_{\substack{\text{Input Parameter}\\ \text{Uncertainty}}} + \underbrace{u_{\text{exp}}^2}_{\substack{\text{Experimental}\\ \text{Uncertainty}}}}. \tag{1.4}$$

Solution verification is discussed in Section 7, input uncertainty is discussed in Section 9.1, and experimental uncertainty is discussed in Section 8. Note that this analysis does not include the three other sources of uncertainty, namely, coding error uncertainty, representation and geometric fidelity uncertainties, and physics and material model fidelity uncertainties. Coding error uncertainty is reduced to a negligible amount through the completion of code verification (see Section 4). Representation and geometric fidelity uncertainties are assessed by estimating the geometric discretization error and are shown to be small (see Section 5). Physics and material model fidelity uncertainties are assumed to be low based on subject matter expert (SME) judgment, as documented in the relevant phenomenon identification and ranking table (PIRT) shown in Section 6.

Applying (1.3) to validation data (see Section 8) and (1.4) to the validation uncertainty evaluated in Section 9.2, the model error δ_{model} can be bounded as

$$\delta_{\text{model}} = \underbrace{E}_{\text{Validation}} \pm \underbrace{u_{\text{val}}}_{\text{Total Uncertainty}}. \tag{1.5}$$

According to ASME V&V 20 Section 6-2, conclusions about the suitability of the model and its implementation can be drawn based on the sizes of E and u_{val}. When $|E| >> u_{\text{val}}$, $\delta_{\text{model}} \approx E$, which means that the modeling error is quite large compared to all other errors and that improvements to the model should be made if δ_{model} is too large to make a decision. When $|E| \leq u_{\text{val}}$, the model error δ_{model} is of the same order as $\delta_{\text{num}} + \delta_{\text{input}} - \delta_{\text{D}}$, which means that the modeling error is within the noise level of numerical, input, and experimental uncertainties. In this case, if δ_{model} is too large to make decisions, efforts should be made to reduce the latter sources of uncertainty.

2. EXAMPLE PROBLEM DESCRIPTION

To develop PCMM workflows representative of realistic scenarios, a problem with coupling through a narrow aperture is needed. Additionally, a problem where experimental data is available for comparison allows for realistic validation calculations. The cylindrical cavity coupling problem documented in [10], often referred to as the Higgins cylinder problem, meets these criteria and also has a reasonably short execution time, allowing for faster testing and debugging of workflows.

2.1. Problem Setup

The cylinder has a 10.16 cm (4 in) inner radius, a 60.96 cm (24 in) inner height, and a 6.35 mm (0.25 in) wall thickness. The cavity walls are solid aluminum with a conductivity of $2.6 \times 10^7 \frac{\text{S}}{\text{m}}$. Midway along the length of the cylindrical wall is an azimuthal slot with a chord length of 5.08 cm (2 in) on both the inner and outer slot walls. The aperture has a width of 0.508 mm. More details on the structure and its construction can be found in [10].

The space outside the cavity is modeled as an infinite open region. Both this region and the interior cavity region are modeled with a lossless free space permittivity and permeability. An electric field integral equation (EFIE) [20] with a resistive boundary condition (conductivity $2.6 \times 10^7 \frac{\text{S}}{\text{m}}$) is imposed on the inner cavity surface. Because losses on the exterior surface have negligible impact on the result, the exterior surface is modeled as a perfect electrical conductor. In order to avoid spurious resonances, a combined field integral equation (CFIE) is applied on the exterior surface, except on elements adjacent to the slot aperture, where the EFIE must be used (descriptions of the CFIE and EFIE implemented in Gemma can be found in Gemma's theory manual [13]). The slot aperture is modeled using Gemma's "thick" slot model with a wall conductivity of $2.6 \times 10^7 \frac{\text{S}}{\text{m}}$ and a depth (cavity wall thickness) of 0.25 in. The incident plane wave has an electric field amplitude of $1 \frac{\text{V}}{\text{m}}$ for convenience. The frequency range simulated runs from 1.12 GHz to 1.15 GHz and captures the first cavity resonance. For more details about the numerical setup, see Appendix A for the input deck used.

The quantity of interest in the problem is the ratio of electric field magnitude at a probe point to the incident field magnitude (which in this case is just the plane wave amplitude, typically set to 1 for convenience). More specifically, the ratio between the magnitude of the normal field $|E^{\perp}|$ at the probe point and the amplitude $|\vec{E}^{\text{inc}}|$ of the incident EM excitation is of interest, where the probe point is on the inner cavity wall on one of the flat end-caps, offset 2.54 cm from the cylinder axis away from the slot aperture. This ratio is usually expressed in dB using the formula

$$20 \log_{10} \frac{|E^{\perp}|}{|E^{\text{inc}}|}. \tag{2.1}$$

In this report this quantity is referred to as "field coupling" or "EM coupling" and is a measure of the ability of exterior EM energy to couple through the cavity walls to the probe location. Note that the quantity in (2.1) is the negative of the "shielding effectiveness" for the enclosure, which is defined in the EMC literature (e.g. in [11]) as

$$10\log_{10}\frac{S^{\text{incident}}}{S^{\text{interior}}}$$

where $S \propto |\vec{E}|^2$ signifies power density. Note that Sandia's EM literature often refers to the quantity in (2.1) as "shielding effectiveness" as it differs only in sign, and so to avoid ambiguity this report prefers the "coupling" terminology. Some of the workflow diagrams, however, still refer to "shielding effectiveness" or "SE", where the term should be understood to signify the value in (2.1).

In this report, the problem is excited by a plane EM wave normally incident to the cylindrical wall at the center of the slot aperture. The field is polarized for maximum coupling, that is, with the electric field perpendicular to the slot length (parallel to the cylinder axis). The setup is diagrammed in Figure 2-1.

As the cylinder is empty with conductive walls, a relatively high quality factor can be expected at the resonant frequencies of the cavity. The high quality factor allows us to test our simulation codes in worst-case coupling scenarios where relatively little energy is dissipated within the cavity compared to the amount entering through the aperture. The ratio between the electric field magnitude at the probe location and that of the incident wave is used to characterize the field coupling of the cavity enclosure, that is, to gauge its ability to shield interior components from external EM environments. Since design, safety, and reliability decisions are made using the field coupling, specifically at resonance peaks, it is the primary quantity of interest (QoI) used in this report.

2.2. Numerical Model

This section describes the geometric and physical input parameters supplied to Gemma in the simulations described in this report.

2.2.1. Mesh Description

The surfaces of interest in the problem are the exterior cylindrical structure boundary and the interior cylindrical cavity boundary. As a slot subcell model is used to calculate wave propagation through the slot aperture, the small surfaces within the aperture are not explicitly modeled, and the slot openings into the exterior infinite region and into the interior cavity region are collapsed into curves of no thickness and discretized as series of bar elements. The surfaces are discretized with flat triangles. In this report, following the general recommendation for accuracy at a given frequency, meshes have element edge lengths of less than one tenth the problem wavelength. Two of these meshes are depicted in Figure 2-2, where all exterior triangle elements that share a node

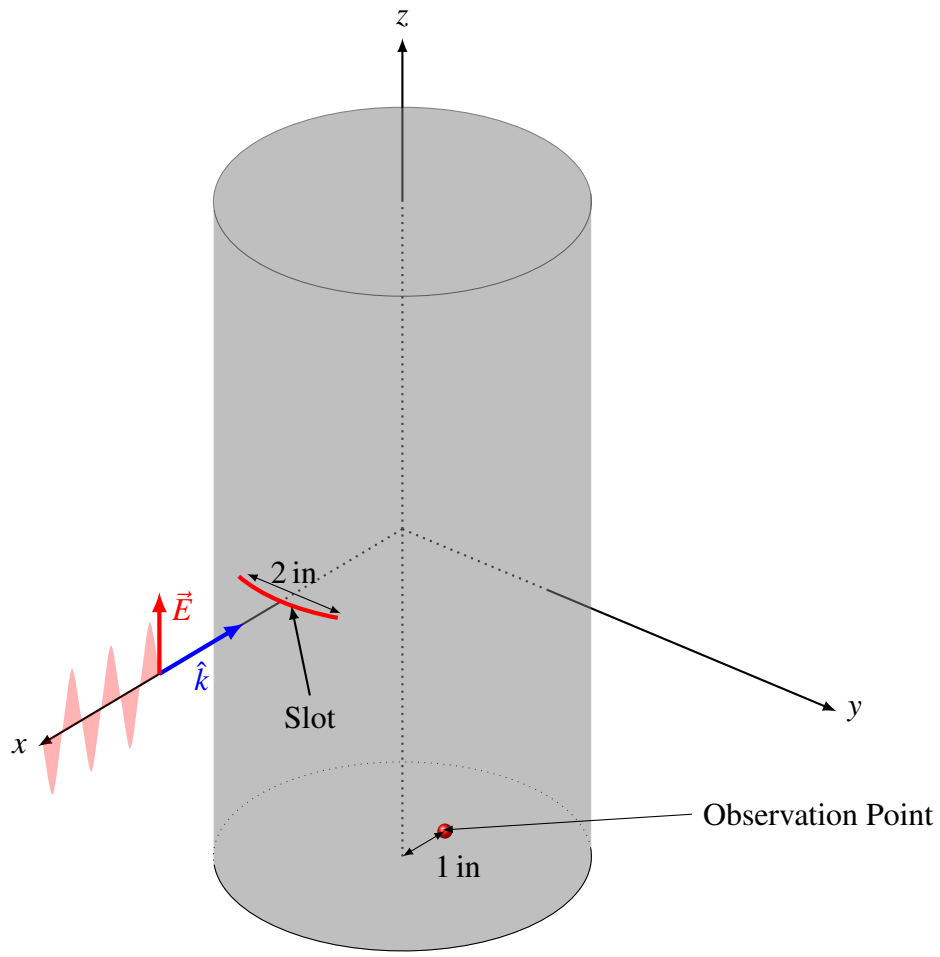

Figure 2-1. Higgins cylinder problem setup. $\vec{E}$ indicates incident field polarization, $\hat{k}$ shows direction of wave propagation.

with the slot aperture curve are colored a lighter shade of blue. At these elements, as mentioned in Section 2.1, an electric field boundary condition must be imposed, and so they are grouped separately from the remainder of the exterior surface. For more details about the mesh, see Appendix B for the meshing file used.

It was noticed after running the analysis that the outer radius in the meshing file does not match the value given in the geometry description in Section 2.1. Additional analysis and spot-checking were carried out, and it was determined that the impact of this discrepancy on the solution was negligible. The surface area was altered by less than 1% and the field coupling by less than 0.1%. Compared to the error from other sources these differences are insignificant.

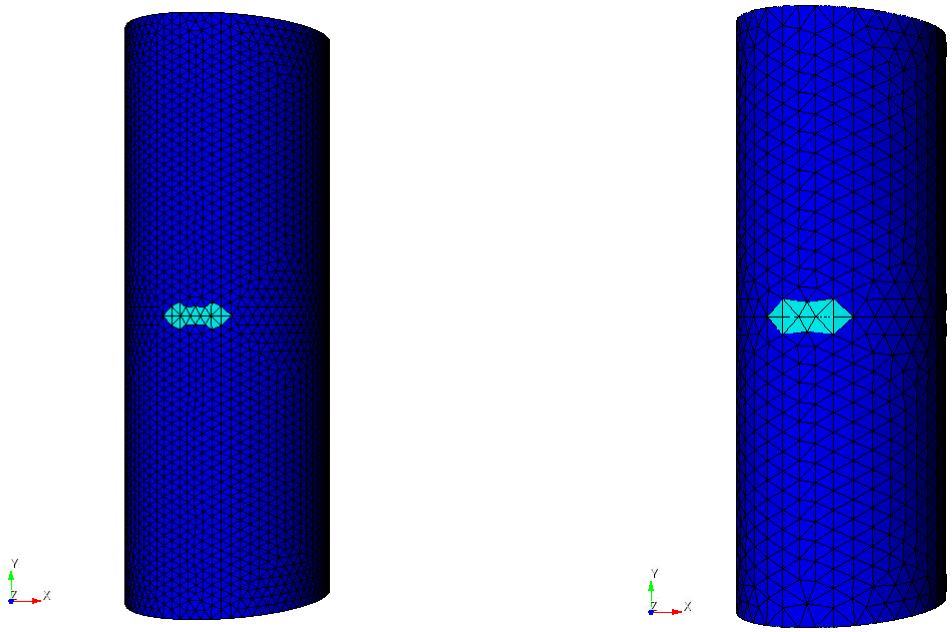

(a) Fine Mesh, $h \approx \frac{\lambda}{30}$ **(b) Coarse Mesh,** $h \approx \frac{\lambda}{15}$

Figure 2-2. A variety of meshes are generated to complete a mesh convergence study. The size h of the mesh elements is chosen based on the problem wavelength, where historically element sizes of less than $\frac{\lambda}{10}$ are considered sufficiently small for accurate discretization at a given frequency.

3. NGW WORKFLOWS

To increase the speed at which an analyst can generate credibility evidence, workflows have been developed for three out of the six PCMM elements. Additionally, for Gemma to interface with NGW, a separate Gemma workflow is developed to run Gemma and parse its output on both the common engineering environment (CEE) and high-performance computing (HPC) machines.

3.1. Gemma Workflow

The first workflow developed was the Gemma workflow, which allows the analyst to specify the input parameters, execute Gemma, and post-process the results. The workflow structure is illustrated in Figure 3-1. The post-processed outputs include the EM coupling data at the cavity resonance peaks, the L2 error norm for a comparison between the simulated frequency response and experimental data (stored in the post-processing workflow), as well as useful plots for reference. This workflow is used as a component in the PCMM workflows to run Gemma and generate quantities of interest. The various pieces of this workflow are described below.

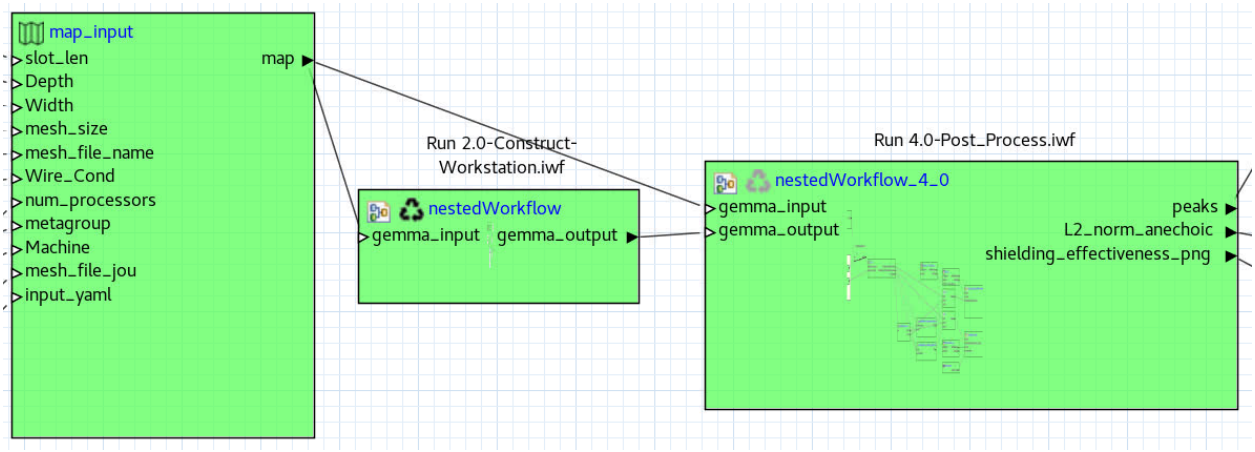

Figure 3-1. Screenshot of the Gemma workflow in NGW.

3.1.1. Construct Workstation Workflow

The construct workstation workflow allows the analyst to run Gemma either locally on the engineering workspace or remotely on the HPCs. This workflow was developed since NGW requires a different "node" depending on which machine the analyst would like to use. In Figure 3-2, the remote nested workflow to run Gemma on an HPC machine requires a config.dat

file, which specifies HPC executable information and an HPC path. These two inputs are not required to run the nested workflow. Future work will allow a third submission location, the non-engineering workspace CEE machines, to ensure these workflows can be used on most Sandia resources.

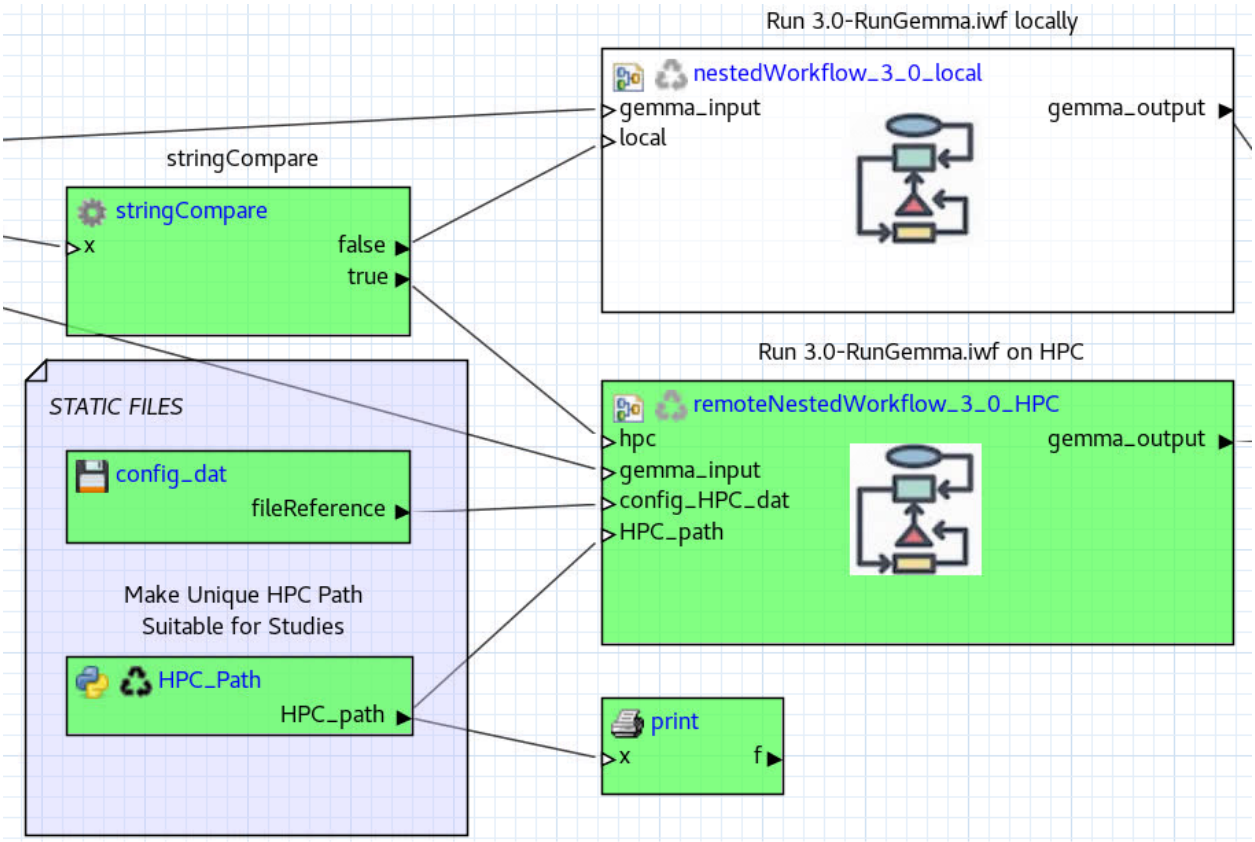

Figure 3-2. Screenshot of the construct workstation workflow in NGW.

Once the analyst selects the desired type of nested workflow (local versus remote), the nested workflow, which is shown in Figure 3-3, runs the meshing workflow and the solve workflow and then returns the field coupling peak value and the field coupling curve.

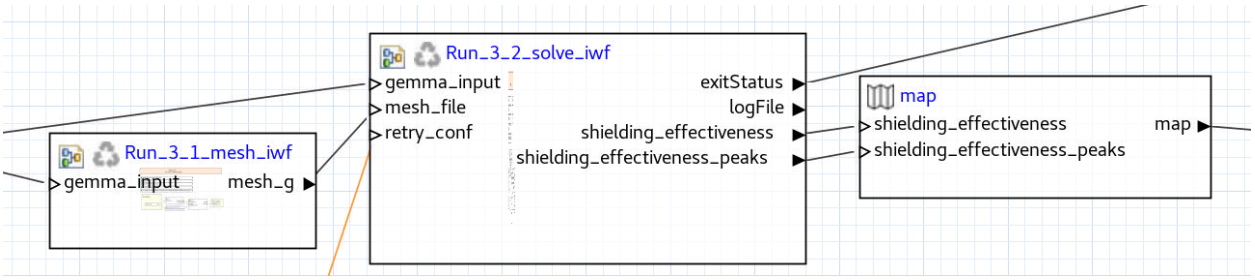

Figure 3-3. Screenshot of the Run Gemma workflow in NGW.

3.1.2. Meshing Workflow

The meshing workflow, illustrated in Figure 3-4, uses a templatized journal file to generate the Genesis mesh using CUBIT. To fill in the templatized journal file, aprepro takes the "gemma_input" variables list and substitutes reference variables into the journal file. This process makes refining or coarsening the mesh or slot discretization relatively simple. Future work would additionally implement the morph mesher into this workflow, making analysis of the impact of defeaturing significantly easier.

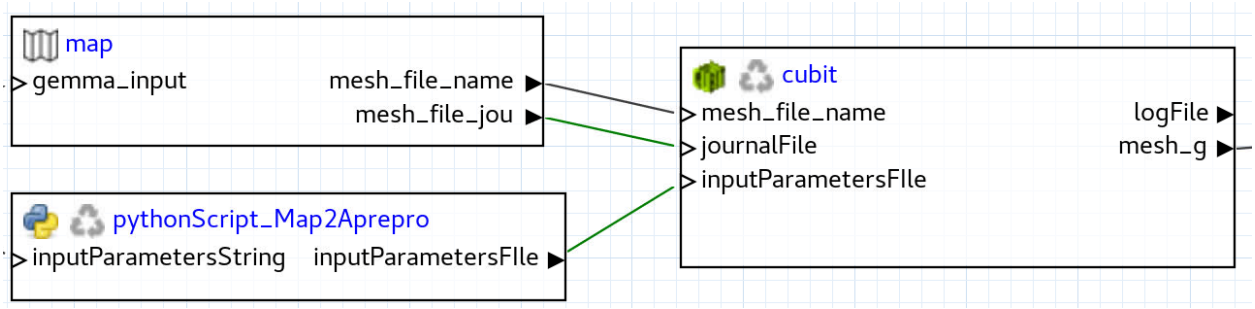

Figure 3-4. Screenshot of the meshing workflow in NGW.

3.1.3. Solve Workflow

Once the Genesis mesh is generated, the solve workflow takes the mesh and the `.yaml` file and runs Gemma on the analyst-specified machine, as shown in Figure 3-5. This workflow takes the longest to finish since this is the bulk of the computational effort. The two key outputs are the rational interpolation plot file, from which the coupling response across the specified frequency range can be readily plotted, and the peaks file, which provides the location and height of each resonant peak detected in the simulation. To reduce the error of rational interpolation, the rational interpolation error tolerance was set to a relative tolerance of $1e^{-3}$, which is significantly lower than other sources of uncertainty.

3.1.4. Post-Processing Workflow

The post-processing workflow, shown in Figure 3-6, plots the frequency response output in the solve workflow and extracts the coupling peaks from the peak file. This workflow could be modified or expanded to perform post-processing for additional analysis types for other quantities of interest.

3.2. Solution Verification Workflow

Now that the Gemma workflow is set up, we can use a Dakota node to control the inputs to Gemma. In the solution verification workflow, shown in Figure 3-7, Dakota sends the Gemma

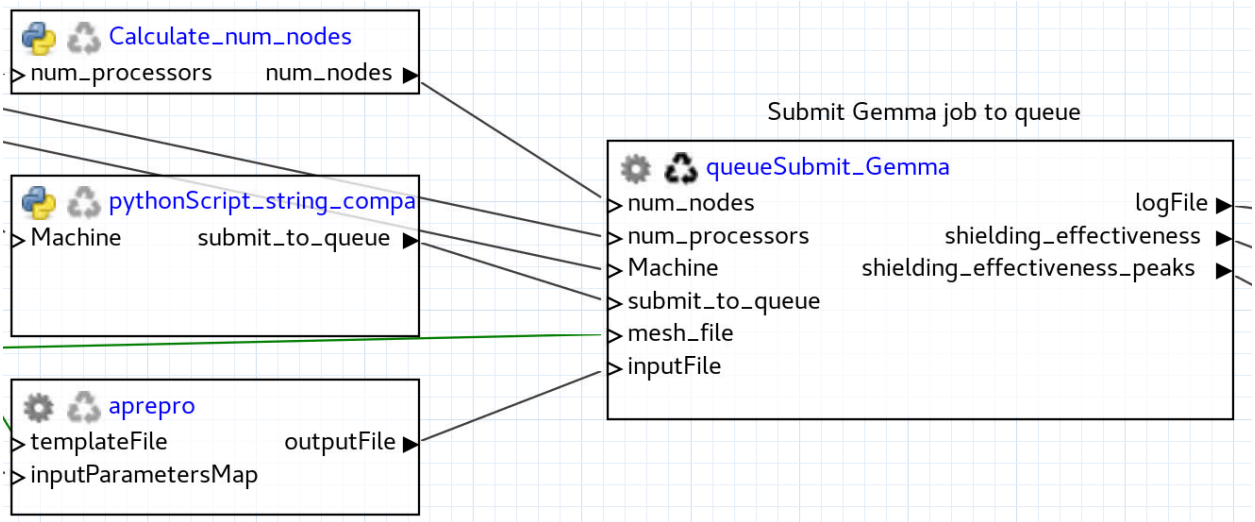

Figure 3-5. Screenshot of the solution workflow in NGW.

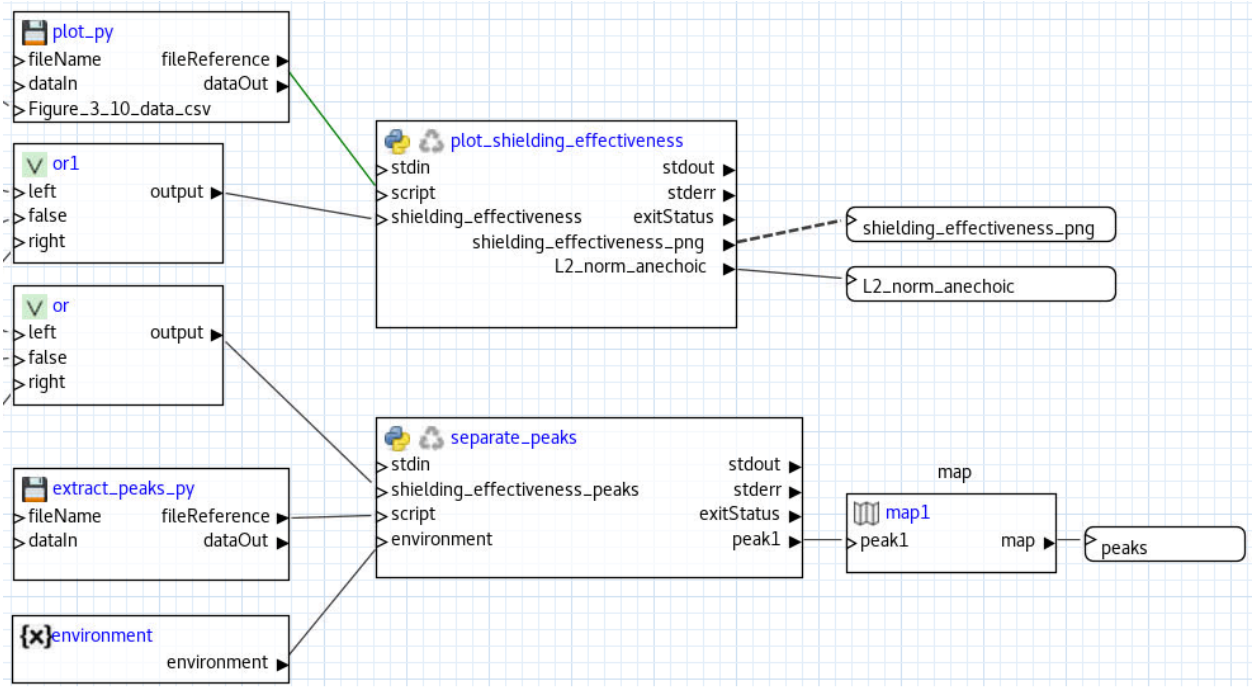

Figure 3-6. Screenshot of the prostprocessing workflow in NGW.

workflow updated values for the mesh size. Since the journal file, which creates the mesh, is templatized, sending updated values allows the analyst to complete a mesh refinement study.

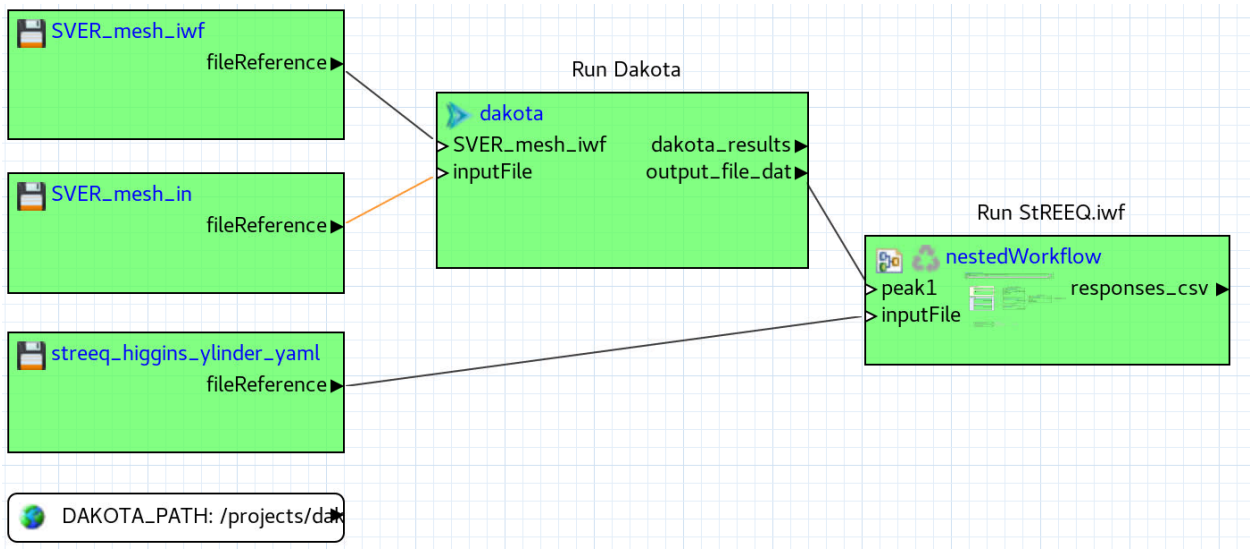

Figure 3-7. Screenshot of the solution verification workflow in NGW.

3.2.1. StREEQ Workflow

Once Dakota runs all of the meshes specified, the program StREEQ is applied to the mesh convergence results to estimate discretization error. The StREEQ workflow, which is shown in Figure 3-8, calculates the median Richardson extrapolation with a 95% bootstrap confidence interval.

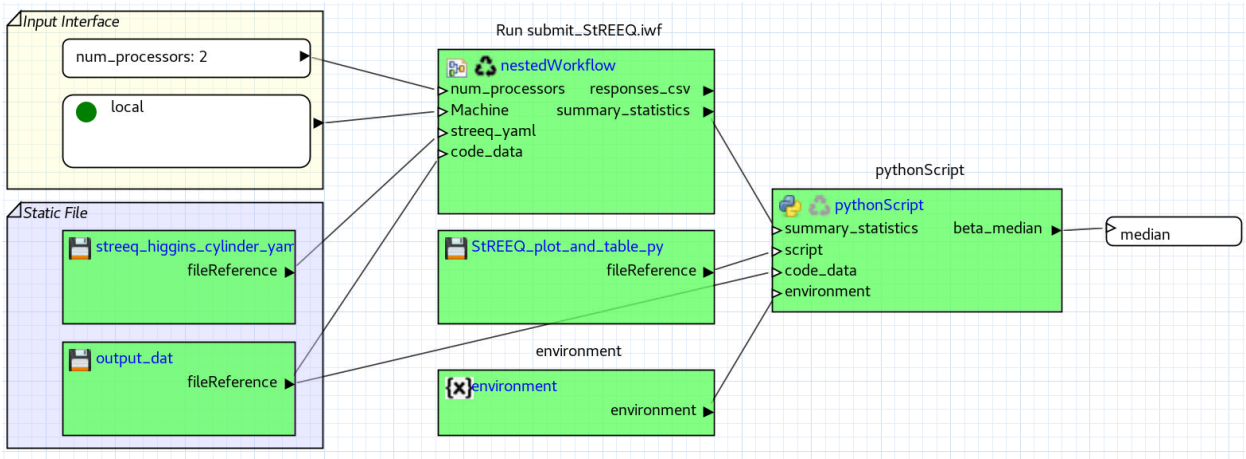

Figure 3-8. Screenshot of the StREEQ workflow in NGW.

3.3. Calibration Workflow

The calibration workflow, illustrated in Figure 3-9, calibrates the slot width to best match the experimental data. Since the slot width is difficult to measure and describe as a single value, the calibration provides a representative slot width that minimizes the uncertainty due to varying width. The workflow runs different widths and collects the L2 norm difference between the computational and experimental data. Using the L2 norm data, an interpolation function is fitted to the L2 norm data and the function is minimized to calculate the optimum slot width. Using the optimum slot width, the difference between the experimental peak coupling level and the Richardson extrapolated median peak values is computed during the validation assessment.

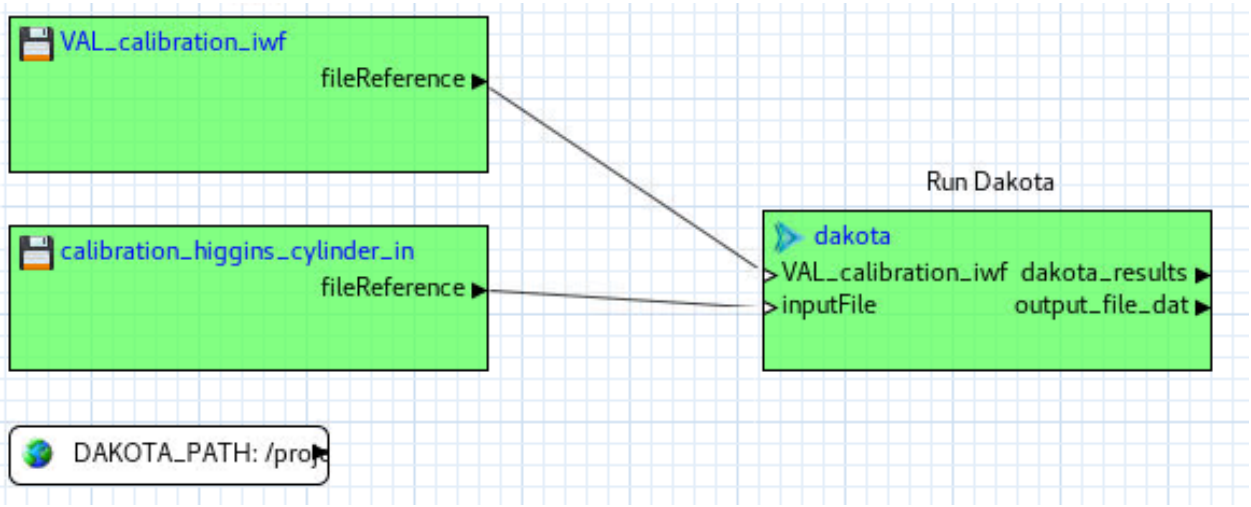

Figure 3-9. Screenshot of the calibration and validation workflow in NGW.

3.4. Input Parameter Uncertainty Quantification Workflow

Figure 3-10 shows the input parameter uncertainty quantification workflow, which computes the local sensitivity for a variety of input parameters. A Dakota node is used to run a parameter sweep to generate Gemma output for each input parameter independently. From this output, the low-resolution (low-res) validation method is used to calculate the corresponding input parameter uncertainty.

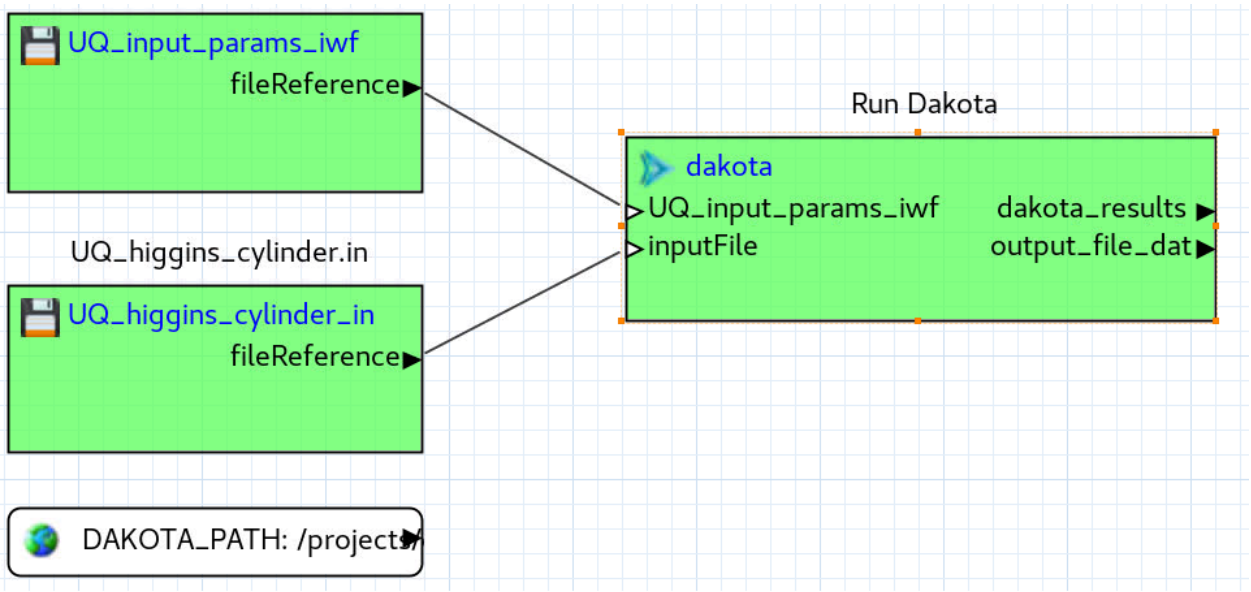

Figure 3-10. Screenshot of the input parameter uncertainty quantification workflow in NGW.

4. CODE VERIFICATION

According to ASME V&V 10 standard [1], verification is the "process of determining that a computational model accurately represents the underlying model and its solution." Additionally, verification is split up into code and solution verification. Code verification is the process of reducing the probability of coding errors, while solution verification estimates the difference between the discretized model and the continuous model. This section focuses on code verification work while Section 7 focuses on solution verification work.

Rather than assessing the uncertainty due to coding errors, code verification's aim is to detect these errors to allow code developers to remove them from the code, which effectively minimizes coding error uncertainty. To minimize the errors, code verification measures the observed order of accuracy and compares it to the theoretical order of accuracy. When the relative difference between the two is less than some tolerance (typically 10%), we assume that minimal coding errors exist within the code. This process is regarded as one of the most sensitive metrics to determine if implementation errors exist within a code [16]. Unfortunately, the field of computational electromagnetics does not have a lot of information about the theoretical order of accuracy or the method of manufactured solutions. This means Gemma's code verification efforts are split into two categories: research and development and code verification testing on Gemma.

4.1. Research and Development

Code verification techniques for EM simulation with the method of moments are the subject of ongoing research and development. Verification researchers at Sandia have recently applied the method of manufactured solutions, which has historically been neglected for electromagnetic radiation problems, to both the EFIE and the magnetic-field integral equations (MFIE) [7, 5, 9, 8, 6]. This work also provides information about the theoretical order of accuracy of different QoIs computed within Gemma, specifically for the EFIE and MFIE. Verification techniques for the CFIE and the slot model are currently being developed.

4.2. Gemma Code Verification Testing

Gemma has a number of code verification tests to ensure the numerical method is implemented correctly. These tests compare Gemma results for multiple mesh refinements and calculate an observed order of accuracy. The observed order of accuracy is then compared against the theoretical order of accuracy. Gemma's order-of-accuracy verification tests have been automated using `vvtest`, a Sandia-developed test harness that wraps around Gemma to generate and

ascicgpu	gemma_cde_v2-gnu-OpenMPI-cuda_9_2-OpenMP-static-Release	0	0	0	0	0	0	134	Sep 03, 2022 - 12:28 UTC
ascicgpu	gemma_cde_v2-gnu-OpenMPI-cuda_9_2-OpenMP-shared-Release	0	0	0	0	0	0	134	Sep 03, 2022 - 12:25 UTC
ascicgpu	gemma_cde_v2-gnu-OpenMPI-cuda_9_2-OpenMP-shared-Debug	0	0	0	0	0	0	121	Sep 03, 2022 - 10:32 UTC
ascic	gemma_cde_v2-gnu-OpenMPI-OpenMP-shared-Debug	0	0	0	0	0	0	121	Sep 03, 2022 - 07:18 UTC
ascic	gemma_cde_v2-gnu-OpenMPI-OpenMP-static-Release	0	0	0	0	0	0	134	Sep 03, 2022 - 05:06 UTC
ascic	gemma_cde_v2-gnu-OpenMPI-OpenMP-static-Release__vvtest	0	0	0	0	0	0	134	Sep 03, 2022 - 04:01 UTC
ascic	gemma_cde_v2-gnu-OpenMPI-OpenMP-shared-Release	0	0	0	0	0	0	134	Sep 03, 2022 - 03:56 UTC

(a) Status of nightly build tests.

Verification *2 builds* [view timeline]

		Test			
Site	Build Name	Not Run	Fail	Pass	Start Time
ascic	sandbox-vvtest_gemma-ascic-cde-openmp-static-release	2	10^{+1}_{-2}	12^{+2}_{-1}	Sep 03, 2022 - 04:37 UTC
ascic	sandbox-vvtest_gemma-ascic-cde-openmp-static-release_revive	0	1	0	Sep 03, 2022 - 05:37 UTC

(b) VVTest status.

Coverage

Site	Build Name	Percentage	LOC Tested	LOC Untested	Date
ascic	gemma_cde_v2-gnu-OpenMPI-OpenMP-shared-Debug	90.41%	26756	2838	Sep 03, 2022 - 07:18 UTC

(c) Code coverage tool computes percentage of code lines covered by unit and regression test suite.

Figure 4-1. Build and test information provided to developers on Gemma's CDash site.

analyze data for a given test. This mesh refinement data is post-process the mesh refinement data with StREEQ [17] and integrated into Gemma's testing dashboard `CDash`. A relative difference of less than some specified tolerance yields a `pass` result. A difference greater than the tolerance is indicated by a `diff` result. If the test does not finish, a `fail` results. Additionally, developers can view `vvtest` pass/fail status on a CDash board along with the status of nightly build testing and an estimate of code test coverage, as shown in Figure 4-1.

For the cylindrical cavity coupling problem, the EFIE and MFIE are used together with the reduced-order slot model. While current Gemma verification testing focuses on the EFIE and MFIE applied to surfaces, verification of the slot model has yet to be addressed. Once the latter is available, it may help to explain the lack of mesh convergence in the cylindrical cavity coupling problem (see Section 7.2). Further details on the test cases in Gemma's `vvtest` suite can be found in Gemma's credibility documentation [15].

5. REPRESENTATION AND GEOMETRIC FIDELITY

Representation and geometric fidelity quantifies the uncertainty due to defeaturing a model and also quantifies the agreement between the model and the as-built geometry. Since the Higgins cylinder is a simple geometric shape, there was no defeaturing of the model and therefore no workflow was created to estimate the associated uncertainty. Additionally, since three-dimensional scans of the experiment were not collected, the uncertainty due to modeling the designed and not the as-built geometry was ignored. However, the geometric discretization error was studied and will be presented at the end of Section 7.2.

6. PHYSICS AND MATERIAL MODEL FIDELITY

The goal of the physics and material model fidelity element of PCMM is to identify the important physics and materials used in the model as well as any modeling. One way of completing this assessment is to complete a phenomenon identification ranking table (PIRT) for both the identification and gap assessment portion of the physics and material model fidelity element. A PIRT involves meeting with subject-matter experts (SME) to fill out the phenomenon list, importance rankings, and adequacy rankings of the PIRT, where math model, code, validation, and model parameter are the four dimensions of adequacy. Based on the level of importance of a given phenomenon, the adequacy columns are colored based on meeting/not meeting the adequacy level required by the importance. The three colors are green, yellow, and red. Green means that the adequacy level is the same level or higher than the importance rank. Yellow means that the adequacy level is one level lower than the importance rank. Red means that the adequacy level is two levels lower than the importance rank. Using a PIRT as a gap analysis tool, the colors highlight areas where the most improvement could be made.

A PIRT assessment was completed for the Higgins cylinder, which is shown in Table 6-1.

Many of the gaps in the PIRT are due to a lack of validation. Additionally, order-of-accuracy testing for the various model implementations would raise the code adequacy rankings to high. Due to the tight interactions between the various phenomena, most parameters are assigned an importance level of high, though future iterations of this PIRT should be completed to determine which phenomenon impacts the QoIs the most. This improvement will allow stakeholders to identify which gaps are most significant.

Table 6-1. FY22 Coupling though a slot PIRT with comments on adequacy

ID	Phenomenon	Imp	Math	Code	Val	Param	Adequacy Comments
A	**Excitation and Interactions with Exterior**						
A1	Incident environment (Plane Wave Model)	H	H	H	H	H	Code implementation simple and easily checked by unit/regression tests. Validation performed with slot-in-infinite-plate and wire/body scattering test cases.
A2	Exterior surface scattering (PEC boundary condition / EFIE / CFIE)	H	H	H	M	H	Cursory validation against monostatic cylinder RCS. No UQ, no extrapolation. Mie series sphere verification gives confidence in MoM implementation for scattering, but does not include sharp edges.
B	**Ports of Entry**						
B1	Slot penetration	H	H	M	M	L	Formal validation needs to be completed. Slot width model parameter is not well understood.
B2	Slot depth resonance	L	H	M	M	L	Not present.
B3	Slot wall losses	H	H	M	M	H	Formal code verification and validation still needed. Sensitivity studies being performed.
C	**Interior of Cavity**						
C1	Material Absorption of EM Energy	L	H	M	L	M	No absorbers in this problem.
C2	Interior wave/-field propagation	H	H	M	L	M	Convergence study and rigorous validation lacking.
C3	High Q Frequency Variation	H	H	M	M	H	Convergence study and rigorous validation lacking.
C4	Wall Losses/Surface Resistance	H	H	M	L	H	Partially verified in regression test comparisons with EIGER and saturation Q test case in `vvtest`. Lacking rigorous validation study.

7. SOLUTION VERIFICATION

Solution verification assesses the numerical uncertainty within a simulation. According to Oberkampf and Roy [16], there are four sources of error that either need to be bounded with an estimate or minimized: discretization error, iteration error, statistical sampling error, and roundoff error.

Since Gemma is a deterministic code, there is no statistical sampling error. Roundoff error is minimized by using double precision variables by default. Moment-method matrix equations for coupling problems cannot be reliably solved by the iterative solvers used in Gemma, and so a direct factor/solve algorithm is used (specifically the lower-upper or "LU" decomposition), thus eliminating iteration error. Therefore, discretization error is the primary source of numerical uncertainty and the focus of this chapter.

7.1. Generation of Solution Verification Data

As discussed in Section 3.2, the solution verification workflow generates EM coupling peak data based on different mesh discretization parameters and post-processes the data to compute a numerical uncertainty that bounds the discretization error. An analyst defines a list of mesh discretization parameters in a Dakota input deck, which tells the Dakota workflow to run Gemma with those meshing parameters. Once the Gemma runs have completed, StREEQ reads in the data and computes the coefficients that best fit the discretization error model,

$$\varepsilon = \beta_1 \times h^{\gamma}, \tag{7.1}$$

where ε is the discretization error, β_1 is a constant coefficient, h is the metric that describes the mesh element size, and γ is the observed order of accuracy. Using this error model, StREEQ calculates the median model fit with a 95% bootstrap confidence interval [17].

7.2. Solution Verification Results

To start, a handful of discretization sizes were selected, and Gemma results were post-processed in StREEQ. Initial results suggested that the mesh was too coarse due to the lack of monotonic convergence, so additional refined meshes were generated. Using the NGW tool, this iterative process was followed until satisfactory results were obtained. The finalized mesh parameters along with the corresponding peak coupling values are shown in Table 7-1.

Table 7-1. Meshing parameters with the corresponding coupling peaks using the CUBIT-specified mesh size parameter.

CUBIT-specified cell size (m)	Peak Coupling [dB]
0.0200	13.92
0.0166	13.76
0.0150	13.85
0.0133	14.33
0.0100	14.50
0.0075	14.46
0.0050	14.37
0.0037	14.17

7.2.1. Peak Coupling Solution Verification Results

A StREEQ analysis using the values in Table 7-1 was completed, and the Richardson extrapolated median value (14.37 dB) as well as the 95% bootstrap confidence interval (11.19 dB, 15.40 dB) is shown in Figure 7-1. To show how refined each mesh was, the corresponding ratios with the wavelength λ are also shown in the figure. Based on historical meshing procedures, a mesh size that is smaller than $\frac{\lambda}{10}$ for the highest frequency is considered to be properly resolved.

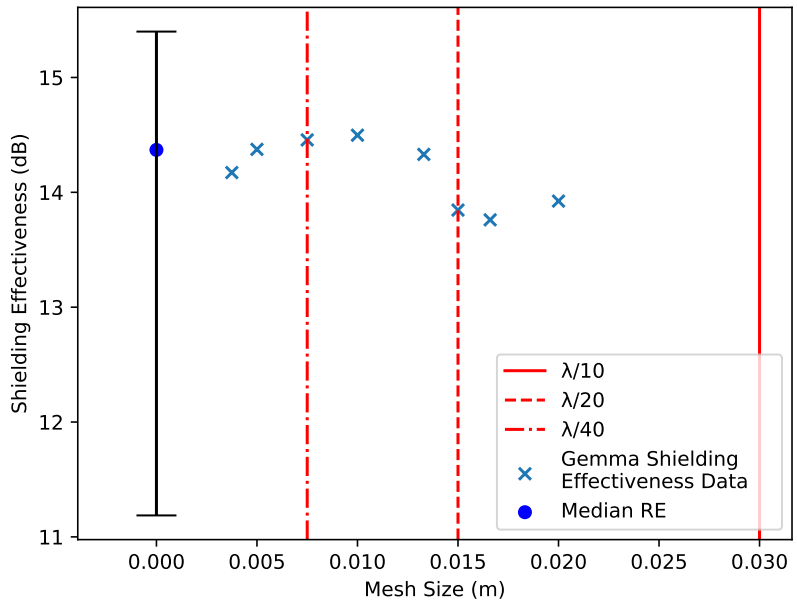

Figure 7-1. Numerical uncertainty for the Higgins cylinder problem using the mesh size specified in the meshing file as the mesh metric.

While the largest difference in coupling is less than one decibel, the median observed convergence rate of 0.97 is not within 10% of the theoretical convergence rate, which is 2.0. This significantly increases the uncertainty to +1 dB/-3 dB. To better understand why this might be the

case, the workflow was used to export additional mesh metrics and post-process the results with StREEQ. The three additional mesh metrics are the average cell size, the quantity $\frac{1}{\sqrt{N_{\text{unknowns}}}}$, and the maximum cell size. The various values of these metrics are tabulated along with the corresponding computed coupling values in Tables 7-2 through 7-3. The coupling results versus the different mesh metrics are shown in Figures 7-2 through 7-3.

Table 7-2. Average cell sizes with the corresponding coupling peaks.

Average cell size (m)	Coupling Peak (dB)
0.0204	13.92
0.0174	13.76
0.0154	13.85
0.0137	14.33
0.0103	14.50
0.0077	14.46
0.0051	14.37
0.0039	14.17

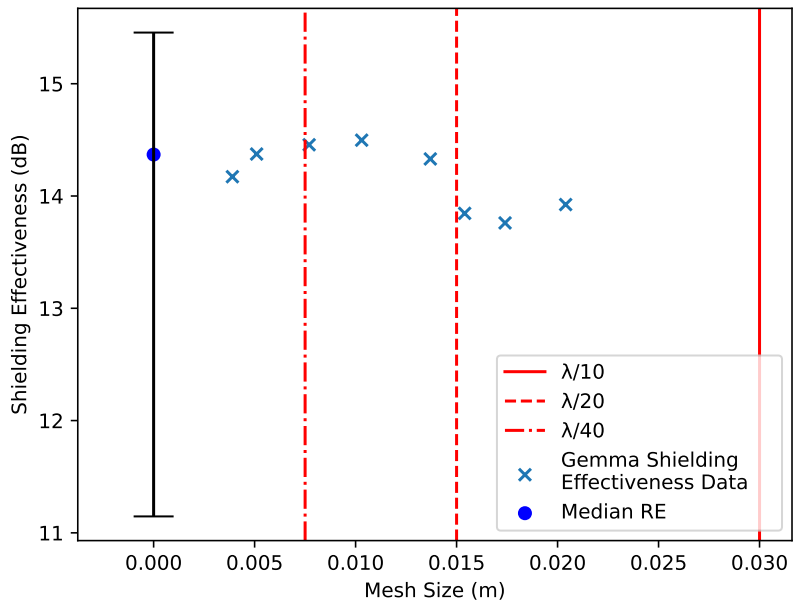

Figure 7-2. Numerical uncertainty for the Higgins cylinder problem using the average cell size as the mesh metric.

The median Richardson extrapolations and 95% bootstrap confidence intervals are not significantly different from those found using the CUBIT-specified mesh size, which means the choice of mesh size metric is not the cause for the degraded convergence rate. Additional work to determine the cause of the degraded convergence rate could include comparison of results computed with rational interpolation to results generated with a uniform frequency sampling across the range. The degraded convergence rate is primarily due both to the lack of code verification evidence for the slot model and to the lack of initial mesh refinement of the slot itself.

Table 7-3. Meshing parameters with the corresponding coupling peaks using the maximum cell size meshing parameter.

Max Cell Size (m)	Peak Coupling (dB)
0.0268	13.92
0.0216	13.76
0.0200	13.85
0.0172	14.33
0.0131	14.50
0.0097	14.46
0.0067	14.37
0.0059	14.17

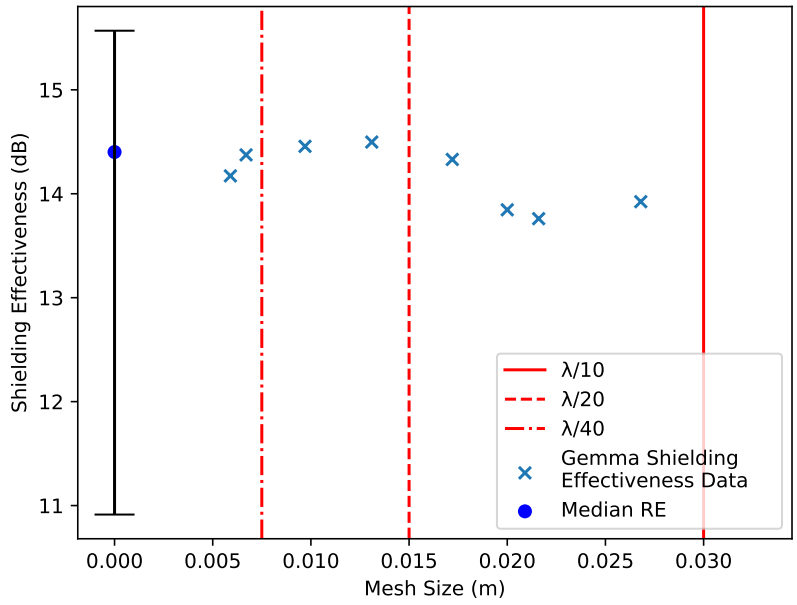

Figure 7-3. Numerical uncertainty for the Higgins cylinder problem using the maximum cell size as the mesh metric.

Since our meshes were generated to be lower than $\lambda/10$, this is only a mesh size approximation for the background mesh and not the mesh size for the slot. Identifying an appropriate mesh size approximation for the slot would help eliminate this issue. The workflows here could be used to generate and process the data to develop an appropriate mesh size approximation.

A key result needed from the solution verification is the response uncertainty due to the estimation of the numerical bias. At present this result is not provided directly from StREEQ, but it can be approximated from the bootstrap confidence intervals using the well-known Chebyshev inequality [3]. For a random variable X following some distribution with finite mean μ and variance σ^2, Chebyshev's inequality states:

$$P(|X-\mu| \geq k\sigma) \leq \frac{1}{k^2}$$

That is, there is only a $1/k^2$ chance that a value lies more than k standard deviations from the mean of the distribution. This inequality can be leveraged to create a confidence interval for the mean that makes no assumption on the shape of the underlying probability distribution, only that the mean and variance exist (e.g., a Cauchy distribution would not be suitable, but any distribution in the exponential family would).

Starting from the confidence interval, we can also construct an approximate estimate of σ. Denote the lower and upper bounds of the interval as $X_{0.025}$ and $X_{0.975}$, respectively. Then equate $X_{0.025} = \mu - k\sigma$ and $X_{0.975} = \mu + k\sigma$, so that the difference between the values is $2k\sigma$. Since the interval is at 95% confidence, we set $1/k^2 = 0.05$ and obtain $k = \sqrt{20}$. This results in an estimate of $\hat{\sigma} = \dfrac{X_{0.975} - X_{0.025}}{2\sqrt{20}}$.

Applying this to the bootstrap confidence interval provided above, we obtain the uncertainty in peak coupling due to estimating numerical bias to be $(15.40 - 11.19)/(2\sqrt{20}) = 0.471\,\text{dB}$. On a variance scale, this is ${u_{\text{num}}}^2 = 0.222\,\text{dB}^2$. This estimate could be improved using knowledge of the shape of the distribution (e.g., Normal). In addition, the need for an approximation can be circumvented entirely by modifying StREEQ so that the bootstrap standard deviation is produced directly, rather than strictly a bootstrap confidence interval.

7.2.2. Geometric Area Solution Verification Results

Lastly, the geometric discretization error is evaluated. When the cylinder is meshed, the surface area of the mesh does not exactly match the area of the cylinder. This difference is referred to as geometric discretization error. However, as the mesh is refined, the sum of the element areas should converge to the exact area of the cylinder. Based on work in Section 3.3.3 of [20], the theoretical order of accuracy for geometric discretization error is 2.0. The observed order of accuracy found here using the solution verification workflow was 1.995, matching the theoretical order of accuracy to three digits, as shown in Figure 7-4.

Since the uncertainty is low and bounds the exact solution, as shown in Table 7-4 and Figure 7-5, and this uncertainty is counted within the total numerical uncertainty, the error due to geometric

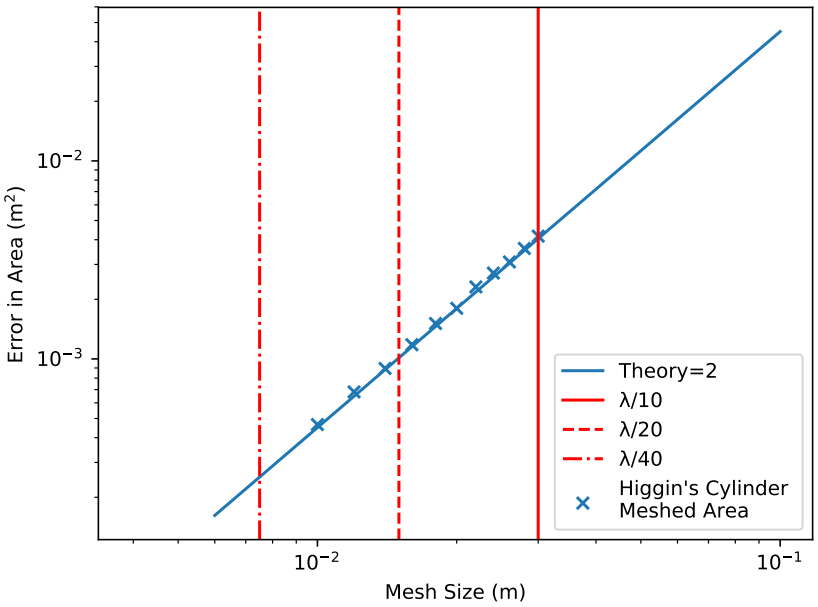

Figure 7-4. Mesh refinement of the area for the Higgins cylinder.

discretization is found not to be a major contributor of numerical uncertainty. This report will therefore focus on other sources of numerical error since they are significantly larger than geometric discretization error.

Table 7-4. Area convergence of the Higgins cylinder.

Parameter	Exact Value	Median	Lower Bound	Upper Bound	Bounded?
Surface Area	0.9475	0.9475	0.9473	0.9477	True
Order-of-Accuracy	2.0	1.995	1.770	2.364	True

For cases where defeaturing does occur, the impact of the defeaturing should be measured. While meshing both the original geometry and the defeatured geometry would be ideal, meshing both geometries is often not practical due to meshing or computational resource limitations. An alternative approach is to measure the impact of a specific defeaturing, such as the impact of rounding a bolt or of smoothing a corner. This approach can identify which defeaturing steps significantly impact solution accuracy and may need to be modified. This process could potentially be streamlined by the NGS Morph meshing software [18].

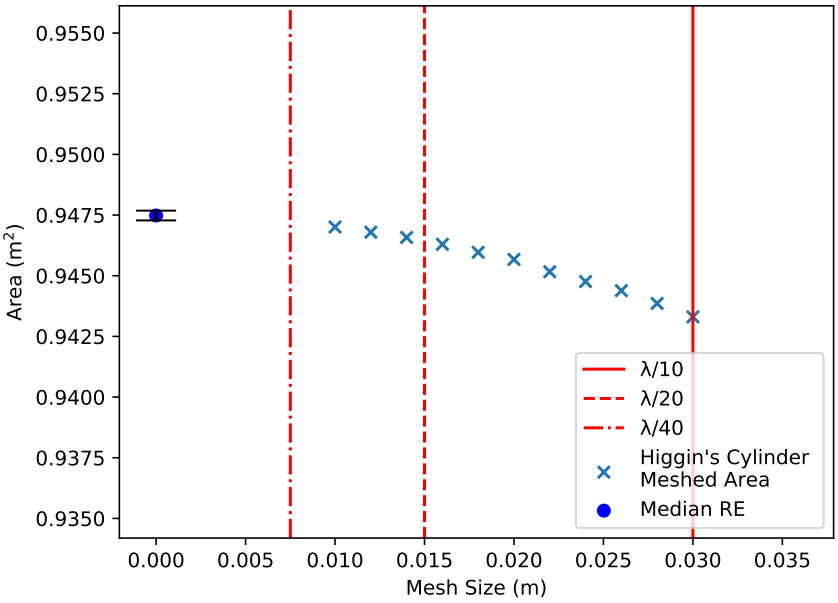

Figure 7-5. Mesh refinement of the area for the Higgins cylinder.

8. CALIBRATION AND VALIDATION

Validation activities assess how well the model matches reality, which requires comparisons to experimental data. Validation is typically preceded by calibration, where the model parameters are tuned to achieve a better match. However, calibration should be completed with subject-matter expert judgment to ensure that the model can extrapolate to areas where the model will be used.

8.1. Calibration

While there are a few parameters that could be used for calibration, slot width was chosen since it's been shown to be the most sensitive parameter in the slot model [14]. Additionally, due to manufacturing techniques, the slot width varies along the length of the slot, making it difficult to quantify the width by a single value. To ensure the model is relevant for predicting coupling across the whole frequency range rather than just at the peaks, the calibration process uses data across the entire range. The Gemma workflow, shown in Figure 3-1, includes a computation of the L2 norm of the difference between the experimental coupling data [10] and the Gemma prediction. This workflow is wrapped by a Dakota workflow, which varies the slot width. The mesh element size was also varied to determine how mesh resolution impacts the calibration process. For this study, the range of slot widths was chosen to be double a reasonable manufacturing tolerance value of 5 mils. Table 8-1 shows the slot width and mesh resolution for each iteration.

Table 8-1. Parameter used for the calibration process.

Case #	Slot Width (cm)	CUBIT-specified cell size (m)
1	0.04	0.01 (Fine)
2	0.045	0.01 (Fine)
3	0.0508	0.01 (Fine)
4	0.055	0.01 (Fine)
5	0.06	0.01 (Fine)
6	0.04	0.02 (Coarse)
7	0.045	0.02 (Coarse)
8	0.0508	0.02 (Coarse)
9	0.055	0.02 (Coarse)
10	0.06	0.02 (Coarse)

Unfortunately, as shown in Figure 8-1, the experimental data near the peak is limited, which artificially reduces the resonance peak height since data was not collected near the actual peak.

Also, the resonance peaks for all Gemma simulations are shifted to the right, impacting the effectiveness of the calibration. Even with these two drawbacks, trends in the data can still be observed. For instance, the coupling levels are shifted up with larger slot widths. Additionally, mesh refinement shifts the simulated peak frequency closer to the experimental peak frequency.

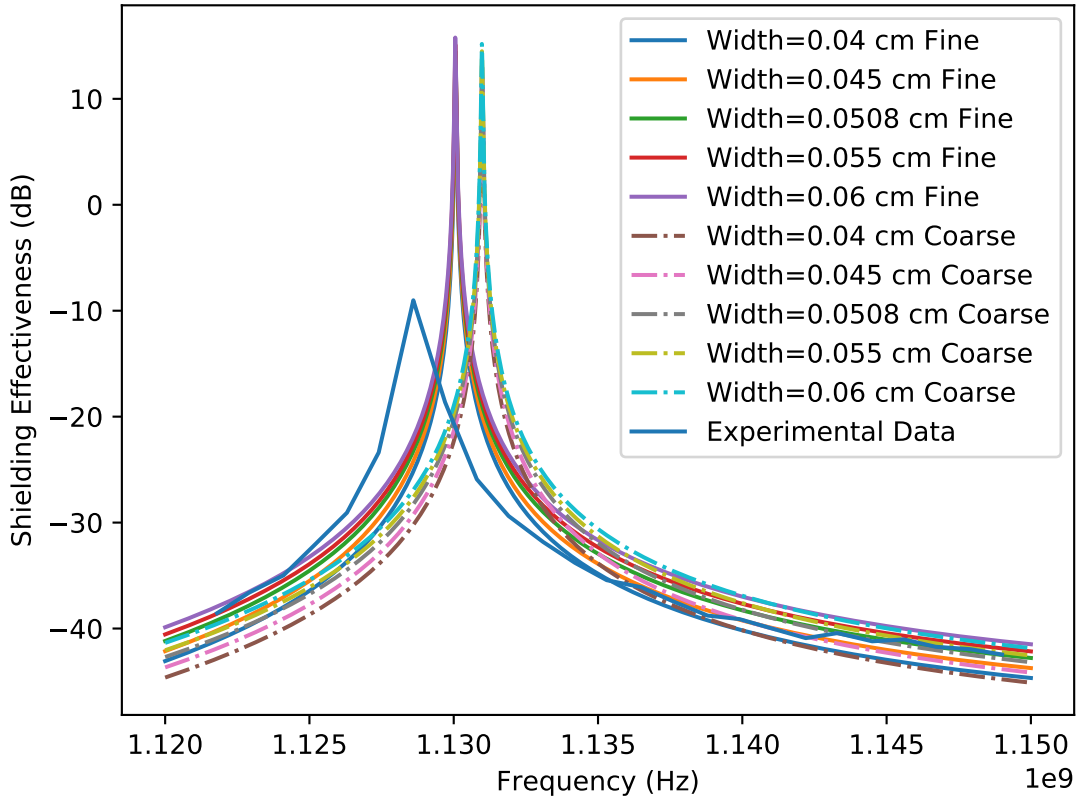

Figure 8-1. Calibration process.

Since the finer mesh results match the experimental data better, the calibration process used the L2 norm values based on these results to determine the optimal slot width. By interpolating and minimizing the L2 norm with respect to the slot width, the optimal width is found to be 0.049 cm, as illustrated in Figure 8-2. This value is used in the validation and uncertainty quantification assessments.

8.2. Validation

Validation assesses the difference between the experimental peak value and the predicted peak value from Gemma (see Eq. 1.1). While a NGW tool was not used for validation, data from the solution verification and calibration workflows contributed to this analysis. The difference between the peak coupling data in [10] and that predicted by Gemma using the calibrated slot width is shown in Table 8-2. Typically, validation data should be different from the calibration data. However, calibration and validation data are taken from the same dataset here solely to demonstrate the workflow.

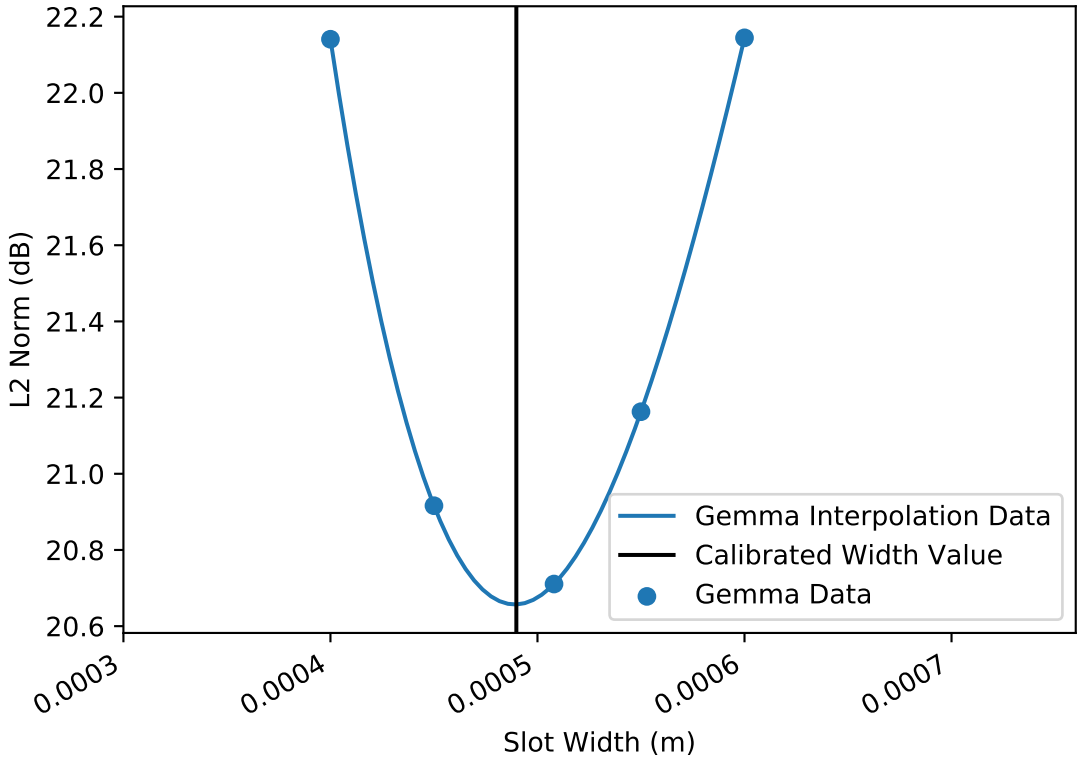

Figure 8-2. Calibration results.

Table 8-2. Validation results after calibration of slot width.

Peak #	Experimental Peak (dB)	Gemma Peak (dB)	Difference (dB)
1	-9.01	14.22	23.23

While the discrepancy between the Gemma prediction and the experimental data is large, it is likely due to lack of frequency resolution in the experimental data. Additionally, experimental uncertainty is not provided, so it is assumed to be zero, which is not realistic. Obtaining experimental measurements (along with measurement uncertainty) that better resolve the resonance peak would likely reduce the disagreement observed here. Calibration of the slot width using a finer mesh would also improve the validation assessment, but less so than obtaining better experimental data.

9. UNCERTAINTY QUANTIFICATION

Previous PCMM sections have focused on the various sources of uncertainty. This section focuses on input parameter uncertainty as well as accumulating all of the known sources of uncertainty to calculate the validation uncertainty.

9.1. Input Parameter Uncertainty

Input parameter uncertainty refers to the uncertainty or variability in the response (in this case, the peak EM coupling level) that arises as a result of varying the input parameters. In the present analysis we consider three inputs: length, width, and depth of the slot. From past investigations, these parameters are believed to have independent effects on SE [4]. Because of this, we employed a centered parameter study, varying only one parameter at a time while holding the others equal to their mean value. The *Low Resolution Validation* (LRV) framework was developed to provide a basic validation and uncertainty quantification analysis for this type of study. LRV is used since it's computationally cheaper than other parameter uncertainty propagation methods and is appropriate to use when the correlation between the parameters is low. Refer to [12] for a more complete mathematical description of this framework.

In addition to being designed exclusively for a centered parameter study, the LRV method also makes the critical assumption of local linearity in the response as the input parameters change. While the global trend in the response will not always be a linear function with the inputs, a suitable restriction of the input space can force local linearity. In this validation study, we assess the linearity of peak EM coupling as a function of the inputs prior to applying LRV using the calibrated slot parameters plus four additional data points per parameter (nominal ± 5 mils and nominal ± 10 mils). A qualitative assessment can be found in Figure 9-1. In this figure, the input variables have been standardized to the $[0,1]$ interval to enable relative comparisons as well as an assessment of linearity. The standardization was performed as $\mathbf{x}_i' = (\mathbf{x}_i - \min \mathbf{x}_i) / (\max \mathbf{x}_i - \min \mathbf{x}_i)$, where $\mathbf{x}_i$ denotes the vector of values for the i^{th} input variable and $\mathbf{x}_i'$ denotes the standardized version of the vector.

Based on Figure 9-1 we can be confident that LRV is a suitable method. A quantitative assessment could be obtained by conducting a lack-of-fit test of the linear approximation (a simple linear regression fit) against a polynomial model of degree 2 or 3. However the results in Figure 9-1 show sufficient linearity. While the peak SE appears to have slight curvature with respect to slot width, the key aspect that local linearity is needed for is obtaining the slope of a least-squares regression, and the observed curvature is small enough that a straight-line approximation is reasonable.

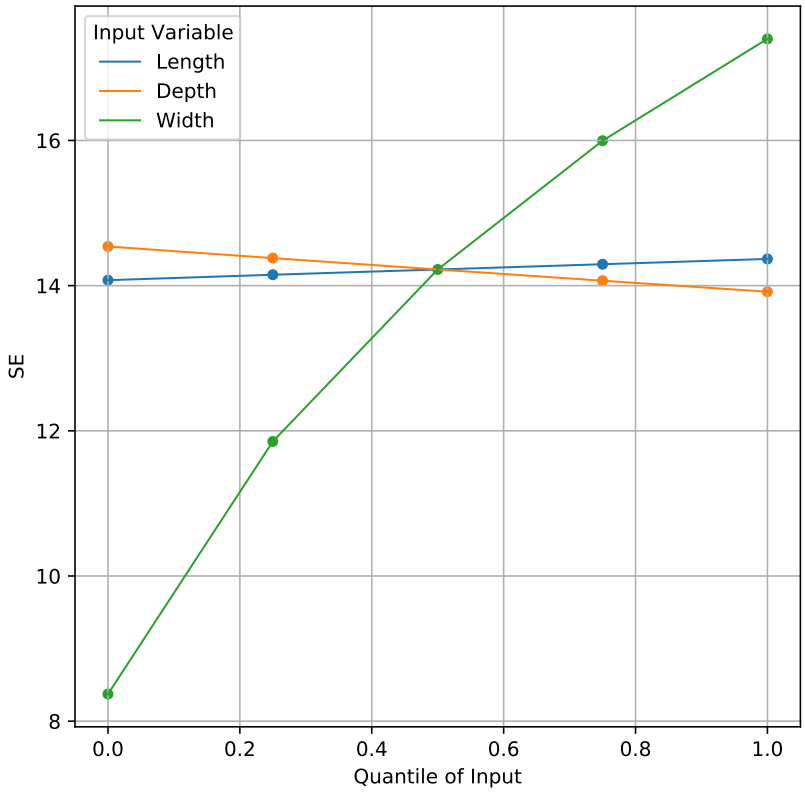

Figure 9-1. Field coupling vs quantile of input parameter.

Another assumption of LRV is that the center point of the input parameters is at least approximately equal to the true (unmeasurable) mean of the input variable. Since a calibration study was performed in advance of the validation study to ensure that the input parameters were centered in approximately the best-fitting location, this assumption was also satisfied.

There are several results that naturally come out of LRV. One such result is a basic UQ analysis. Figure 9-1 can be interpreted as a main effects plot, and indicates that slot width has the most dramatic impact on the EM coupling prediction. In addition, LRV produces an estimate of the variability in EM coupling as a function of the input variation, and this value is the sum of variation contributions due to each of the input parameters. From these we can compute the *percent contribution* of each input parameter to the total uncertainty due to input parameters. These results are provided in Table 9-1, which gives both the percent contribution as well as the estimated uncertainty (variance) in field coupling due to each input variable. Again, we observe that the slot width is (by far) the largest contributor to the uncertainty in field coupling.

Table 9-1. Response uncertainty (variance) and associated percent contribution of each input parameter.

	Percent	SE Var
Length	0.001074	0.021287
Width	0.994032	19.705415
Depth	0.004895	0.097028

The total uncertainty in field coupling due to input parameter variation is the sum of the individual response uncertainties in Tab 9-1, which is $u_{\text{input}}{}^2 = 19.82373$.

9.2. Combining Uncertainties using ASME VVUQ 20

Uncertainty quantification for the Higgins cylinder is a culmination of assessing code bug uncertainty (code verification), geometric discretization uncertainty (representation and geometric fidelity), model fidelity uncertainty (physics and material model fidelity), numerical uncertainty (solution verification), experimental uncertainty, and input parameter uncertainty. These uncertainties were either minimized (code bug uncertainty, geometric discretization uncertainty, and model fidelity uncertainty), assumed to be zero (experimental uncertainty), or assessed (numerical uncertainty and input parameter uncertainty). Using the uncertainties that were assessed and (1.4), the validation uncertainty is computed to be

$$u_{\text{val}} = \sqrt{\underbrace{u_{\text{num}}{}^2}_{\substack{\text{Solution}\\ \text{Verification}}} + \underbrace{u_{\text{input}}{}^2}_{\substack{\text{Input Parameter}\\ \text{Uncertainty}}} + \underbrace{\cancelto{0}{u_{\text{exp}}{}^2}}_{\substack{\text{Experimental}\\ \text{Uncertainty}}}} = 4.477. \tag{9.1}$$

By assessing the size of the validation uncertainty compared to the validation error from Section 8.2, conclusions can be drawn about the predictive ability of Gemma's simulation of coupled EM fields. Recall that the validation error was $E = 23.23$ dB, which is much larger than the validation uncertainty $u_{\text{val}} = 4.477$. Hence, clearly, the observed validation error is not within a $\pm 1 u_{\text{val}}$ bound. However, it is not uncommon for a random variable to produce a value more than one standard deviation away from the mean. If we assume that Gemma's prediction model is unbiased (so that the expected validation error is zero), we can again make use of the Chebyshev inequality to determine how unlikely of an event the value $E = 23.23$ represents. Recall that Chebyshev's inequality is given by:

$$P(|X - \mu| \geq k\sigma) \leq \frac{1}{k^2}$$

We now equate the validation discrepancy to the random variable X, and under the assumption that Gemma is unbiased set $\mu = 0$. So we take $k = E/u_{\text{val}}$, which yields $k = 5.19$ and $1/k^2 = 0.0371$. Therefore, based on the Chebyshev inequality, the probability of the observed validation error E (or a validation error E' where $|E'| > |E|$) is at most 3.71%. Since we assumed that Gemma was unbiased, this probability can be interpreted as a p-value testing the hypothesis of unbiasedness.It is common in Statistics to compare a p-value to some threshold such as 0.05 or 0.01 (though this is not strictly necessary, as a p-value is simply measuring the probability of an event; comparing to a specified threshold is only a means of turning a continuous measure into a binary value for decision-making).

This probability is sensitive to knowledge of the underlying probability distribution of E. When using the Chebyshev inequality we make no assumption of the probability distribution except that it has a finite mean and variance. If we were to assume, say, a normal distribution for E, the corresponding probability would be $2.13e-5\%$. For this reason, a characterization of the distribution of E would be useful.

9.3. Interpretation of Results

While an event with probability 3.71% is not unreasonable to occur, if we are not assuming a distribution we do not know whether 3.71% or $2.13e-5\%$ is the true probability of the event $E = 23.23$, and regardless would prefer the observed validation error to represent a more likely scenario. There are several means by which this can be achieved. First, the model could be improved. If there are known deficiencies or inaccuracies in the model, correcting or reducing these could result in improved accuracy. However, it is not a given that there are any aspects of the model to improve. If the real-world process is a highly noisy process, then even a perfectly unbiased model could often result in predictions deviating significantly from experimental data, leading to a large validation error.

This leads naturally to the second approach of estimating the experimental uncertainty. As noted we assumed that the $u_{\text{exp}} = 0$, which may not be reasonable. If there is experimental uncertainty, then ignoring it makes E appear to be more unlikely than it is in reality. Conducting additional

experimentation to characterize u_{exp} would result in an increased u_{val}, one consequence of which would one that the observed E would not appear to be such an unlikely event.

A third approach is to increase the range of the input parameters. For the present validation experiment the range of the input variables was set based on a validation study, and these ranges are believed to represent a $\pm 1\sigma$ bound on each input parameter. Revisiting the selected input space could result in a conclusion that the 1σ bounds are wider than were assumed. This is a second natural result of the LRV analysis, which acts in some ways as a secondary calibration. For instance if we want to constrain the validation error to be within $\pm 1 u_{\text{val}}$, the LRV analysis suggests that the input parameter uncertainties (which is reflected in the range in the inputs) needs to be increased by 454%. This is a dramatic inflation of the input uncertainty, though this would be somewhat mitigated by incorporation of experimental uncertainty.

Finally, it is worth noting that the observed results show that the experimental peak coupling is lower than the Gemma-calculated peak, which is a deviation in a "good" direction (Gemma *underestimating* the experimental result would be an error in a "bad" direction). The LRV framework is designed to bound the experiment using a 2-sided interval. But if only a bound on the upper side is consequential, it may be possible to modify the methodology of LRV to consider this scenario.

10. CONCLUSIONS

Assessing the model credibility for models within Gemma is an important step in using Gemma for qualification evidence. Using PCMM is an effective way to assess the model credibility. Since generating PCMM evidence is labor intensive, setting up workflows to iterate certain PCMM activities speeds up the evidence generation process as well as the investigative process when the data is suggesting counterintuitive results. This report focuses on developing three workflows to speed up the PCMM activities: solution verification, which computes the numerical uncertainty; calibration/validation, which computes the validation comparison error and reports the experimental uncertainty; and uncertainty quantification, which computes the uncertainty in the output due to uncertainties in the input parameters. Based on the results shown in Section 9.2, the validation comparison error is much larger than the uncertainties quantified in this report. If the validation comparison error is too large for the intended application, this means one of two things: either the model form error is large and should be reduced or there are uncertainties that are not being quantified (e.g. experimental uncertainty). Using the workflows developed in this work, additional analysis can be quickly completed if the improvements to the model are made or if better experimental data with uncertainty is collected.

BIBLIOGRAPHY

[1] ASME. *V&V 10-2019: Standard for Verification and Validation in Computational Solid Mechanics*. Tech. rep. American Society of Mechanical Engineers, 2020.

[2] ASME. *V&V 20-2009: Standard for Verification and Validation in Computational Fluid Dynamics and Heat Transfer*. Tech. rep. American Society of Mechanical Engineers, 2009.

[3] Robert Bartoszynski and Magdalena Niewiadomska-Bugaj. *Probability and statistical inference*. John Wiley & Sons, 2020.

[4] Salvatore Campione et al. "Developing Uncertainty Quantification Strategies in Electromagnetic Problems Involving Highly Resonant Cavities". In: *Journal of Verification, Validation and Uncertainty Quantification* 6.4 (Aug. 2021). ISSN: 2377-2158. DOI: 10.1115/1.4051906. URL: https://doi.org/10.1115/1.4051906.

[5] Brian A. Freno, Neil R. Matula, and William A. Johnson. "Manufactured solutions for the method-of-moments implementation of the electric-field integral equation". In: *Journal of Computational Physics* 443 (2021), p. 110538. ISSN: 0021-9991. DOI: https://doi.org/10.1016/j.jcp.2021.110538. URL: https://www.sciencedirect.com/science/article/pii/S0021999121004332.

[6] Brian A. Freno et al. "Characterization and Integration of the Singular Test Integrals in the Method-of-Moments Implementation of the Electric-Field Integral Equation". In: *arXiv preprint arXiv:1911.02107* (2020).

[7] Brian A. Freno et al. "Characterization and integration of the singular test integrals in the method-of-moments implementation of the electric-field integral equation". In: *Engineering Analysis with Boundary Elements* 124 (2021), pp. 185–193. ISSN: 0955-7997. DOI: https://doi.org/10.1016/j.enganabound.2020.12.015. URL: https://www.sciencedirect.com/science/article/pii/S0955799720303283.

[8] Brian A. Freno et al. "Code-verification techniques for the method-of-moments implementation of the electric-field integral equation". In: *Journal of Computational Physics* 451 (2022), p. 110891. ISSN: 0021-9991. DOI: https://doi.org/10.1016/j.jcp.2021.110891. URL: https://www.sciencedirect.com/science/article/pii/S0021999121007865.

[9] Brian A. Freno et al. "Symmetric triangle quadrature rules for arbitrary functions". In: *Computers & Mathematics with Applications* 79.10 (2020), pp. 2885–2896. ISSN: 0898-1221. DOI: https://doi.org/10.1016/j.camwa.2019.12.021. URL: https://www.sciencedirect.com/science/article/pii/S0898122119305954.

[10] Matthew B. Higgins and Dawna R. Charley. *Electromagnetic Radiation (EMR) coupling to complex systems : aperture coupling into canonical cavities in reverberant and anechoic environments and model validation.* Tech. rep. SAND2007-7931. Albuquerque, NM: Sandia National Laboratories, 2007.

[11] D.A. Hill et al. "Aperture excitation of electrically large, lossy cavities". In: *IEEE Transactions on Electromagnetic Compatibility* 36.3 (1994), pp. 169–178. DOI: 10.1109/15.305461.

[12] Casey Jelsema et al. *Gemma V&V/UQ/Credibility Activities - FY20 Progress*. Tech. rep. SAND2021-6172. Albuquerque, NM: Sandia National Laboratories, 2021.

[13] W. A. Johnson et al. *Gemma Electromagnetic Theory Manual*. Tech. rep. Albuquerque, NM: Sandia National Laboratories, 2022.

[14] Aaron M. Krueger. *News Note: ASC researchers at Sandia developed a streamlined workflow to predict electromagnetic radiation shielding effectiveness for the W80-4 system*. Tech. rep. SAND2021-15082 O. Albuquerque, NM: Sandia National Laboratories, 2021.

[15] Aaron M. Krueger, Casey M. Jelsema, and Robert A. Pfeiffer. *Model-Level Credibility Evidence*. Tech. rep. To be published. Albuquerque, NM: Sandia National Laboratories, 2023.

[16] William L. Oberkampf and Christopher J. Roy. *Verification and Validation in Scientific Computing*. Cambridge University Press, 2010. DOI: 10.1017/CBO9780511760396.

[17] Gregg A. Radtke et al. "Robust verification of stochastic simulation codes". In: *Journal of Computational Physics* 451 (2022), p. 110855. ISSN: 0021-9991. DOI: https://doi.org/10.1016/j.jcp.2021.110855. URL: https://www.sciencedirect.com/science/article/pii/S0021999121007506.

[18] Matthew L Staten et al. *Massively Parallel Tet Meshing With Size-Dependent Feature Capture on CAD Models.* Tech. rep. Sandia National Lab.(SNL-NM), Albuquerque, NM (United States); Sandia …, 2018.

[19] V&V/UQ and Credibility Processes Team. *What is Predictive Capability Maturity Model?* Tech. rep. SAND2016-7399. Albuquerque, NM: Sandia National Laboratories, 2016.

[20] Karl F Warnick. *Numerical analysis for electromagnetic integral equations*. Artech House, 2008.

APPENDIX A. Gemma Input Deck

```
%YAML 1.1
---

Gemma-dynamic:

  Global:
    Description: 2 prisms with slot between them
    Solution type: matrix

  Mesh:
    File:
      File Type: Exodus
      File Name: {mesh_file_name}

  Property:
    slot:
      Slot:
        Width: {Width}
        Depth: {Depth}
        Conductivity: {Slot_Cond}
    inside_surface_probe:
      Resistive metal:
        Region normals toward: 2Inside (R2)
        Region normals away: PEC
        Sigma: {Surf_Cond}
    inside_surface:
      Resistive metal:
        Region normals toward: 2Inside (R2)
        Region normals away: PEC
        Sigma: {Surf_Cond}
    outside_attached_slot:
      Perfect metal:
        Equation: pec_efie
        Normals: in
        Region:  1Outside (R1)
    outside_remainder:
      Perfect metal:
        Equation: pec_cfie
        Normals: in
        Region:  1Outside (R1)

  Region:
    1Outside (R1):
      Homogeneous:
        Material: air
```

```
    2Inside (R2):
      Homogeneous:
        Material: air

  Material:
    air:
      Simple:
        Epsilon: [1.0, 0.0]
        Mu: [1.0, 0.0]

  Excitation:
    Excitation 1:
      Plane wave spherical:
          Region:  1Outside (R1)
          Incident field:
            H field:
              H theta:     [0.0026544,0.0]
              H phi:   [0.0,0.0]
          Propagation angle:
              Theta:    [0.0]
              Phi:      [0.0]

  Frequency:
    Rational interpolation:
      Frequency lower bound: 1.12e9
      Frequency upper bound: 1.15e9
      Probe coordinate: [0.0, -0.30050, -0.0254]
      Probe test direction: [0.0, 1.0, 0.0]
      Relative tolerance: 1e-3
      Maximum points: 31

  Output:
    File: output

...
```

APPENDIX B. Gemma Mesh File

```
# Build the Higgins slotted cylinder with one slot
# Cylinder is aligned with y axis with slot centered about z axis
#
# Units are meters

reset
reset aprepro
#{include("params.apr")}

# mesh size
# frequency of 5 GHz
# {delta=mesh_size}

# slot length
# Length is projected slot length; actual arc length is slightly longer
# Slot length is set on inner radius and adjusted on outer radius
# to give same arc length for slot inlet and outlet
#{slot_len_inch=slot_len}          # length in inches
#{_slotlen=0.0254*slot_len_inch}
# Dimensions of cavity interior
# radius=4 in, h=24 in
#{_ri=0.1016}
#{_hi=0.6096}
# Dimensions of cavity exterior
# radius=4.25 in, h=24.5 in
#{_ro=0.1076}
#{_ho=0.6223}


create cylinder height {_ho} radius {_ro}
create cylinder height {_hi} radius {_ri}

# rotate cylinder to align with y axis
rotate volume all angle 90 about x
# create vertical curves to decompose surfaces
create curve vertex 1 2
create curve vertex 3 4
# Save ids of curves
#{cvo=5}
#{cvi=6}

# create horizontal curves to decompose for slot
curve 2 copy move x 0 y {0.5*_ho} z 0
curve 4 copy move x 0 y {0.5*_hi} z 0
#{cho=7}
```

```
#{chi=8}

# Make curves to decompose cylinder symmetrically
curve {cvi} {cvo} copy rotate 180 about y

# Decompose for slot on inside and outside

# Adjust outside slot length to match slot length on inside
#{thi=asind(0.5*_slotlen/_ri)}   # angle in degrees for inside slot
#{tho=_ri/_ro*thi}              # match slot arc lengths
curve {cvi} copy rotate {-90+thi} about y
curve {cvi} copy rotate {-90-thi} about y
curve {cvo} copy rotate {-90+tho} about y
curve {cvo} copy rotate {-90-tho} about y

imprint volume 1 2 with curve with num_parent=0
delete curve with num_parent=0

# create triangle with centroid at probe location (1 in from axis)
#{_vertex1=Id("vertex")}
create vertex 0.0 {-0.5*_hi} {-0.0254-(delta/sqrt(3))}
create vertex { 0.5*delta} {-0.5*_hi} {-0.0254+(0.5*delta/sqrt(3))}
create vertex {-0.5*delta} {-0.5*_hi} {-0.0254+(0.5*delta/sqrt(3))}
create curve vertex {_vertex1+1} {_vertex1+2}
create curve vertex {_vertex1+2} {_vertex1+3}
create curve vertex {_vertex1+3} {_vertex1+1}
imprint volume 2 with curve with num_parent=0
delete curve with num_parent=0

# create slot surface
#{_curv1=Id("curve")}
create curve vertex 30 40
create curve vertex 23 33
create surface curve 24 {_curv1+1} 44 {_curv1+2}
merge curve in volume 1 with curve in volume 3
merge curve in volume 2 with curve in volume 3

# reverse normals for inside so they point into cavity
# (In Cubit 15.3 only works correctly if done before meshing)
reverse surface in volume 2

# Mesh
surface all size {delta}
surface all scheme trimesh
surface in vol 3 scheme map

# mesh slot
curve with length<0.0065 in volume 3 interval 1
curve 24 44 size {delta}/2
mesh surface in volume 3

# mesh inside and outside surfaces
mesh surface in volume 2 with has_scheme "trimesh"
mesh surface in volume 1 with has_scheme "trimesh"
```

```
100
101 block 1 surface in volume 3                              # slot
102 block 2 surface with area<{delta*delta} in volume 2   # probe element
103 block 3 surface with area>{delta*delta} in volume 2   # cavity inside
104 block 4 tri in volume 1 in node in curve in volume 3 # outside attached to
       slot
105 block 5 tri in volume 1 except tri in node in curve in volume 3 # rest of
       outside
106 #
107 block 1 name "slot"
108 block 2 name "inside_surface_probe"
109 block 3 name "inside_surface"
110 block 4 name "outside_attached_slot"
111 block 5 name "outside_remainder"
112
113 export mesh "higgins_cylinder_meters.g" overwrite
```

DISTRIBUTION

Email—Internal

Name	Org.	Sandia Email Address
Gary Pena	1350	gepena@sandia.gov
Joe D. Kotulski	1352	jdkotul@sandia.gov
William L. Langston	1352	wllangs@sandia.gov
Alexander Moreno	1352	amoreno@sandia.gov
Jeff Osterberg	1352	jaoster@sandia.gov
Alden R. Pack	1352	arpack@sandia.gov
Robert A. Pfeiffer	1352	rapfeif@sandia.gov
Luis San Martin	1352	lsanmar@sandia.gov
Andy Huang	1355	ahuang@sandia.gov
Matthew R. Glickman	1462	mrglick@sandia.gov
Lauren L. Beghini	1544	llbeghi@sandia.gov
Kevin J. Dowding	1544	kjdowdi@sandia.gov
Brian A. Freno	1544	bafreno@sandia.gov
Aaron M. Krueger	1544	amkrueg@sandia.gov
Blake Lance	1544	blance@sandia.gov
Kyle D. Neal	1544	kneal@sandia.gov
Casey M. Jelsema	5574	cmjelse@sandia.gov
Matthew D. Smith	5574	mdsmith@sandia.gov
Maher Salloum	8739	mnsallo@sandia.gov
Technical Library	1911	sanddocs@sandia.gov

Hardcopy—Internal

Number of Copies	Name	Org.	Mailstop
1	Technical Library	9536	0899

Sandia National Laboratories

Sandia National Laboratories is a multimission laboratory managed and operated by National Technology & Engineering Solutions of Sandia LLC, a wholly owned subsidiary of Honeywell International Inc., for the U.S. Department of Energy's National Nuclear Security Administration under contract DE-NA0003525.